

Ultrahigh Stable Methanol Oxidation Enabled by a High Hydroxyl Concentration on Pt Clusters/MXene Interfaces

Jiexin Zhu,[#] Lixue Xia,[#] Ruohan Yu,[#] Ruihu Lu, Jiantao Li, Ruhan He, Yucai Wu, Wei Zhang, Xufeng Hong, Wei Chen, Yan Zhao, Liang Zhou, Liqiang Mai,* and Ziyun Wang*



Cite This: *J. Am. Chem. Soc.* 2022, 144, 15529–15538



Read Online

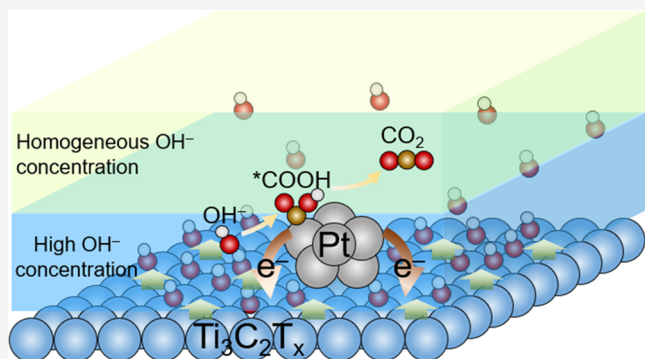
ACCESS |

Metrics & More

Article Recommendations

Supporting Information

ABSTRACT: Anchoring platinum catalysts on appropriate supports, e.g., MXenes, is a feasible pathway to achieve a desirable anode for direct methanol fuel cells. The authentic performance of Pt is often hindered by the occupancy and poisoning of active sites, weak interaction between Pt and supports, and the dissolution of Pt. Herein, we construct three-dimensional (3D) crumpled $\text{Ti}_3\text{C}_2\text{T}_x$ MXene balls with abundant Ti vacancies for Pt confinement via a spray-drying process. The as-prepared Pt clusters/ $\text{Ti}_3\text{C}_2\text{T}_x$ ($\text{Ptc}/\text{Ti}_3\text{C}_2\text{T}_x$) show enhanced electrocatalytic methanol oxidation reaction (MOR) activity, including a relatively low overpotential, high tolerance to CO poisoning, and ultrahigh stability. Specifically, it achieves a high mass activity of up to $7.32 \text{ A mg}_{\text{Pt}}^{-1}$, which is the highest value reported to date in Pt-based electrocatalysts, and 42% of the current density is retained on $\text{Ptc}/\text{Ti}_3\text{C}_2\text{T}_x$ even after the 3000 min operative time. In situ spectroscopy and theoretical calculations reveal that an electric field-induced repulsion on the $\text{Ptc}/\text{Ti}_3\text{C}_2\text{T}_x$ interface accelerates the combination of OH^- and CO adsorption intermediates (CO_{ads}) in kinetics and thermodynamics. Besides, this $\text{Ptc}/\text{Ti}_3\text{C}_2\text{T}_x$ also efficiently electrocatalyze ethanol, ethylene glycol, and glycerol oxidation reactions with comparable activity and stability to commercial Pt/C.



INTRODUCTION

The development of fuel cells has been considered an important approach to achieve carbon neutrality.^{1–6} Owing to their high energy density, low cost, and convenient transport, direct methanol fuel cells (DMFCs) are promising devices for energy conversion in portable electronic devices and electronic vehicles.^{7–9} High dosages of precious metal catalysts and poor operation durability are the inevitable obstacles to large-scale commercialization.^{10–14} As one of the most promising catalysts, extensive efforts are devoted to controlling the nanostructures and compositions of platinum-based materials, thus improving the specific activity and durability.^{15–17} Constructing Pt–M alloys like PtNi,^{18,19} PtPd,²⁰ PtRu,¹⁷ PtCu,²¹ and PtFe,²² with specific ratios between Pt and M, as well as diverse nanostructures like nanowires,²³ nanosheets,²⁴ specific facets,^{25,26} and core–shell²⁷ structures, have been implemented to tune the adsorption strength of the CO intermediate (CO_{ads}). The amelioration behaviors can be derived from the strong absorption capacity of additional metal units to hydroxyl groups (OH_{ads}), which act as an oxidant to bind and activate CO_{ads} .^{17,28,29} However, even with the optimization strategies mentioned above, only the Pt sites around the addition metal units are capable of tolerating CO poisoning, while the Pt sites far from the

additional metal atom are still stuck with CO_{ads} due to the loss of connection with additional metals. Consequently, extra strategies beyond utilizing an external water oxidation catalyst are urgently needed.

Placing Pt units on the substrates, which can promote the dissociative adsorption process of H_2O molecules to form OH_{ads} is considered to be an effective method to improve durability.^{28,30,31} Huang et al.²⁸ designed Pt– $\text{Ni}(\text{OH})_2$ –graphene electrocatalysts, in which $\text{Ni}(\text{OH})_2$ serves as an assistant for water dissociation and graphene provides high electric conductivity. Nevertheless, even though the Pt nanocrystals grow on both $\text{Ni}(\text{OH})_2$ nanoparticles and graphene, only those loaded on $\text{Ni}(\text{OH})_2$ can resist CO poisoning. In addition, Pt units may also nucleate and grow outside the substrates. Hence, the substrates' ability to adsorb and anchor Pt units plays an important role in constructing uniform supported catalysts. MXenes are a group of two-

Received: April 15, 2022

Published: August 9, 2022



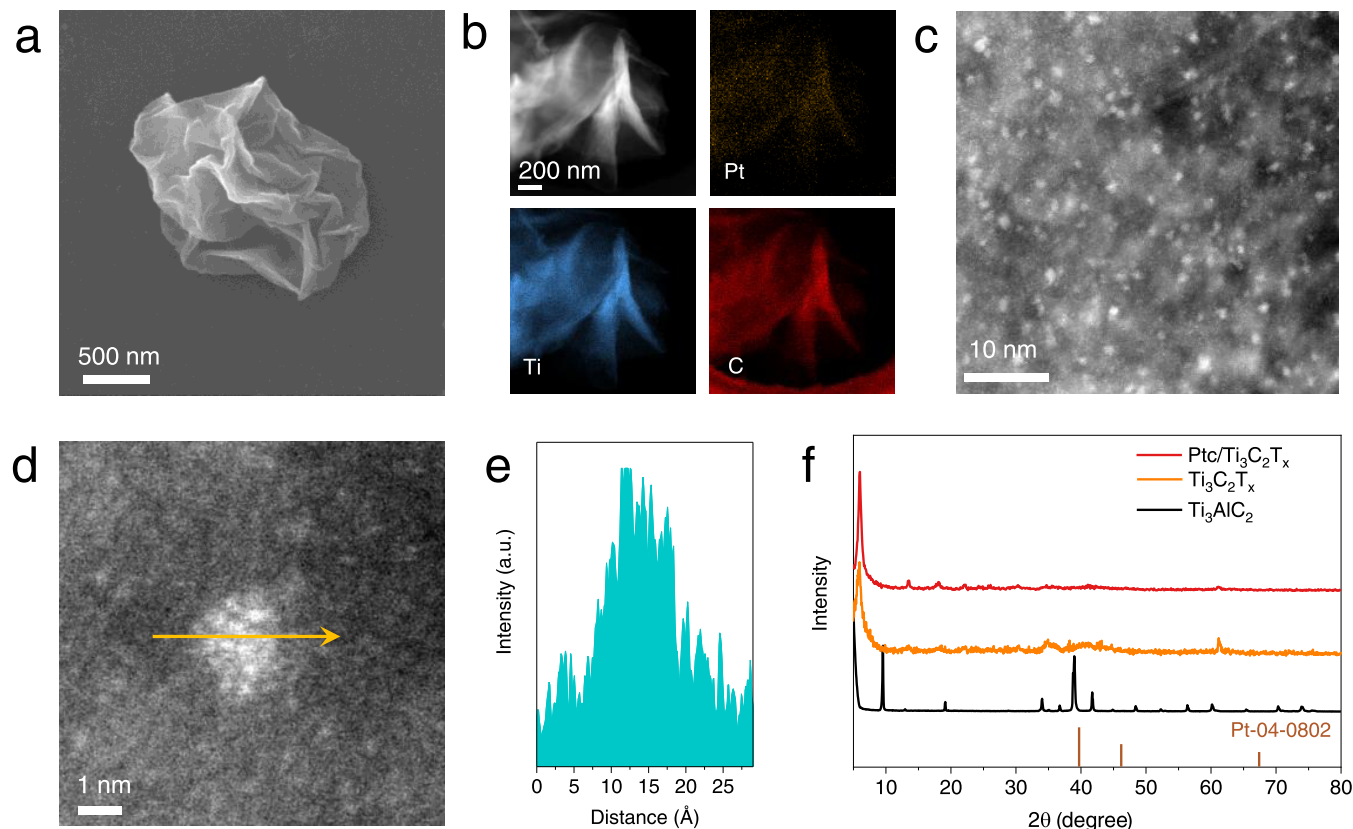


Figure 1. (a) Scanning electron microscopy (SEM) image of Ptc/Ti₃C₂T_x. (b) HAADF-STEM image and corresponding energy-dispersive spectrometry (EDS) mapping of Ptc/Ti₃C₂T_x. (c) HAADF-STEM image of Ptc/Ti₃C₂T_x. (d, e) HAADF-STEM image and corresponding linear intensity profiles of Ptc/Ti₃C₂T_x. (f) XRD patterns of Ti₃AlC₂, Ti₃C₂T_x, and Ptc/Ti₃C₂T_x.

dimensional materials with high conductivity and rich terminal groups ($-O$, $-OH$, $-F$), showing great promise in energy storage and conversion.^{32–39} After being etched by HF solutions, atomic Ti defects are formed on the surface and have a negligible effect on the metallic conductivity.⁴⁰ It has been confirmed that single metal atoms could be located at the atomic defects and form a strong metal–carbon bond.^{33,35} Therefore, MXenes represent promising potential as a support for metal electrocatalysts.

Herein, we construct three-dimensional (3D) crumpled Ti₃C₂T_x MXene balls decorated with ultrafine Pt clusters via the spray-drying method for a high-efficiency methanol oxidation reaction (MOR). A 3D crumpled structure suppresses the agglomeration of Ti₃C₂T_x and maximizes the exposure of Pt sites. With the assistance of spectroscopies and density functional theory (DFT) calculations, the charge transfer between Pt clusters and Ti₃C₂T_x is revealed. Also, in situ spectroscopy and electrochemical characterizations uncover the ion migration behavior near the catalyst surface, which deeply affect the methanol oxidation performance of Pt sites. The resultant Ptc/Ti₃C₂T_x catalysts show a lower overpotential and about twofold increases in mass activity compared to commercial 20% Pt/C and achieve a huge improvement in durability.

RESULTS AND DISCUSSION

Synthesis and Structural Characterization of Electrocatalysts. Ti₃C₂T_x MXene nanosheets were prepared through etching Al layers from the Ti₃AlC₂ MAX phase using HF solution etching, followed by tetramethylammonium hydroxide

(TMAH) intercalation and ultrasonic stripping.^{33,41,42} As shown in Figures S1 and S2, the accordion-like Ti₃C₂T_x MXene nanosheets with a hole-rich morphology were obtained due to the etching of HF. During the process, a small portion of Ti atoms on the surface peeled off with the etched Al layers, where the Ti-deficient sites were created.⁴⁰ To decorate Pt clusters onto Ti₃C₂T_x, a certain proportion of chloroplatinic acid hexahydrate solutions and Ti₃C₂T_x nanosheet aqueous solutions was mixed uniformly and then delivered to spray-drying equipment. The drying process of two-dimensional (2D) materials is usually accompanied by an obvious agglomeration phenomenon, causing the blocking of active sites. Using the spray-drying technique,⁴³ the ultrafast solvent vaporization process converts the 2D nanosheets into 3D crumpled balls (Figures 1a and S3), which effectively reduces the occurrence of agglomeration. With the reducibility of Ti defects,³⁵ Pt⁴⁺ would be reduced and bonded strongly with C atoms. The high-angle annular dark-field scanning transmission electron microscopy (HAADF-STEM) images and the corresponding energy-dispersive X-ray (EDX) elemental mappings also manifest that the Pt units are evenly distributed on the Ti₃C₂T_x surface (Figure 1b). When the mass fraction of Pt units reduces to 0.6 wt %, Pt single atoms would be formed on the Ti₃C₂T_x surface (namely, Pts/Ti₃C₂T_x). As shown in Figure S4, Pt atoms are anchored on the same path as Ti atoms, and significant Ti defects can be found on the surface, indicating that the Pt atoms occupy the Ti-deficient sites. As the Pt loading increases, the Pt clusters show up but are still in a good distribution (Figure 1c), which benefits from the ultrafast drying process from spray-drying. The uniform size of

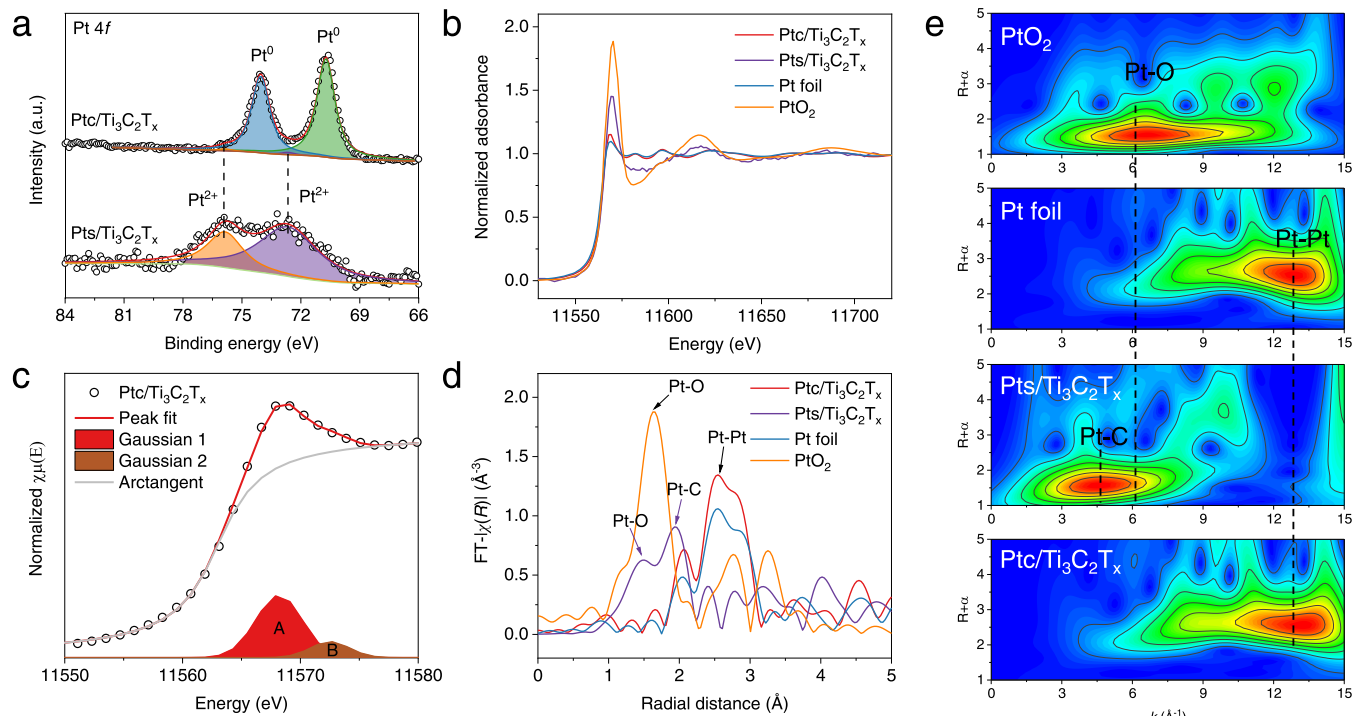


Figure 2. (a) High-resolution Pt 4f XPS spectra of Ptc/Ti₃C₂T_x and Pts/Ti₃C₂T_x. (b) Normalized Pt L₃-edge XANES for Ptc/Ti₃C₂T_x, Pts/Ti₃C₂T_x, Pt foil, and PtO₂. (c) White line peak fitting analyses of Pt L₃-edge XANES spectra of Ptc/Ti₃C₂T_x. (d) FT $k_3\chi(R)$ Pt L₃-edge EXAFS spectra for Ptc/Ti₃C₂T_x, Pts/Ti₃C₂T_x, Pt foil, and PtO₂. (e) WT for the Pt L₃-edge EXAFS signals for Ptc/Ti₃C₂T_x, Pts/Ti₃C₂T_x, Pt foil, and PtO₂.

about 1.5 nm for Pt clusters was recorded by linear intensity profile analysis (Figure 1d,e), and no peaks of Pt can be found in X-ray diffraction (XRD) patterns because of the extra-small size (Figure 1f).

Electronic States of Pt Units in Ptc/Ti₃C₂T_x. X-ray photoelectron spectroscopy (XPS) and X-ray absorption spectroscopy (XAS) were adopted to analyze the electronic states of Pt single atoms and clusters on the surface of Ti₃C₂T_x. The high-resolution XPS spectra of the Pt 4f spectrum in Figure 2a indicate that the oxidation state of Pt in Pts/Ti₃C₂T_x may be +2, while Pt(0) is dominant in Ptc/Ti₃C₂T_x. However, when the size of Pt is reduced to a single atom, the highest occupied molecular orbital (HOMO) is shifted down with respect to the Fermi level (E_F), which enlarges the band gap and stabilizes the initial state, thus resulting in the positive shift in binding energy. So, the valence state of Pt in Pts/Ti₃C₂T_x should be higher than 0 but lower than +2.⁴⁴ The C 1s spectrum of Ti₃C₂T_x and Ptc/Ti₃C₂T_x consists of three peaks set at the binding energies of 282.9, 284.5, and 286.9 eV, which can be assigned to C–Ti/Pt, C–C, and C–O, respectively (Figure S5). The high-resolution Ti 2p spectrum shows four pairs of representative and similar peaks in Ti₃C₂T_x and Ptc/Ti₃C₂T_x (Figure S6).⁴⁵ It is worth noting that the peak intensity of TiO_{2-x}F_{2x} in Ti₃C₂T_x is higher than that of Ptc/Ti₃C₂T_x, meaning that the filling of Ti defect by Pt units reduces the surface instability of Ti₃C₂T_x, thus reducing the degree of surface oxidation. A similar phenomenon also exists in the O 1s spectrum (Figure S7). The X-ray absorption near-edge structure (XANES) spectra of Pt L₃-edge reveal the intensity of the white line peak for Pts/Ti₃C₂T_x and Ptc/Ti₃C₂T_x between those of Pt foil and PtO₂ (Figure 2b). The average oxidation number of Pt can be obtained by integrating the white line intensity of the Pt L₃-edge.⁴⁶ From the fitting results (Figures 2c and S8), the white line area of Ptc/Ti₃C₂T_x

is located between Pt foil and Pts/Ti₃C₂T_x, and the fitted average oxidation number of Pt in Ptc/Ti₃C₂T_x is 0.58. However, considering the size effect, the valence state of the Pt cluster should be less than +0.58 but higher than 0.⁴⁴ Moreover, an additional fitted peak (peak B) can be detected in Ptc/Ti₃C₂T_x which may be ascribed to the excitation of electrons from the C/O 2p shell to the Pt 5d shell, suggesting that the Pt clusters are in an electron-deficient state. Figure 2d shows the Fourier transform extended X-ray absorption fine structure (FT-EXAFS) for Pt L₃-edge of Ptc/Ti₃C₂T_x, Pts/Ti₃C₂T_x, and references. The spectra of Ptc/Ti₃C₂T_x display the main peak at 2.5 Å, which can be assigned to the first shell of Pt–Pt scattering.^{47,48} Two main peaks at about 1.9 and 1.5 Å of Pts/Ti₃C₂T_x are associated with Pt–C and Pt–O,³³ respectively, and the Pt–Pt contribution is absent. EXAFS wavelet transform (WT) analysis of the Pt L₃-edge was adopted to further verify the coordination structure. As shown in Figure 2e, only one intensity maximum at ~4.5 Å⁻¹ related to the Pt–C coordination is observed in Pts/Ti₃C₂T_x.³⁵ The intensity of Pt–O coordination is located between 4 and 8 Å⁻¹ in PtO₂. Combining the surface-adsorbed oxygen-containing group on Ti₃C₂T_x and the results of EXAFS, we may identify that Pt in Pts/Ti₃C₂T_x is coordinated with C and O atoms. Ptc/Ti₃C₂T_x exhibits a contour map similar to Pt foil with a distinct intensity maximum at ~13 Å⁻¹ corresponding to the Pt–Pt coordination, and no discernible intensity of Pt–C/O coordination can be identified. However, from the HAADF-STEM image in Figure 1c, we can find many Pt single atoms on the Ti₃C₂T_x surface. Thus, the Pt single atoms and Pt clusters coexist and the absence of Pt–C/O coordination in WT may be attributed to the very high intensity of Pt–Pt coordination.

Electro-oxidation of Methanol. To evaluate the electrochemical activity of Ptc/Ti₃C₂T_x, we choose MOR as a model

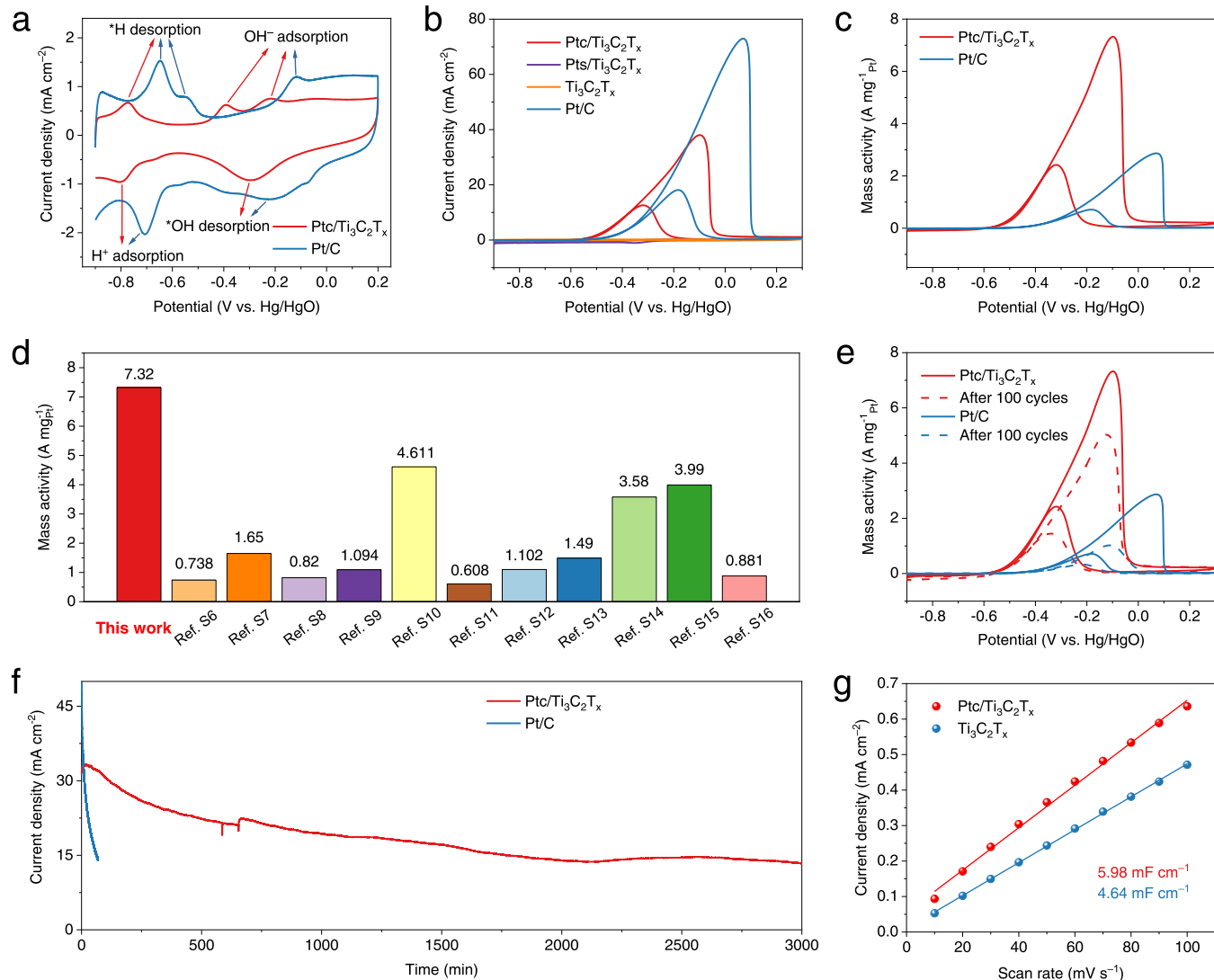


Figure 3. (a) CV curves of Ptc/Ti₃C₂T_x and Pt/C in 1 M KOH. (b) CV curves of Ptc/Ti₃C₂T_x, Pts/Ti₃C₂T_x, Ti₃C₂T_x, and Pt/C in 1 M methanol/1 M KOH. (c) Mass activity of Ptc/Ti₃C₂T_x and Pt/C. (d) Histograms of the mass and specific activities of different catalysts. (e, f) Durability test of Ptc/Ti₃C₂T_x and Pt/C in 1 M methanol/1 M KOH. (g) ECSA test of Ptc/Ti₃C₂T_x and Ti₃C₂T_x.

reaction. Pt-based electrocatalysts usually exhibit superior activity toward the electrocatalytic MOR, but the activity is easily blocked by CO poisoning.^{28,49} We compare the MOR activity of Ptc/Ti₃C₂T_x and Pts/Ti₃C₂T_x with commercial 20% Pt/C catalysts in alkaline electrolytes. Before conducting the MOR test, Ptc/Ti₃C₂T_x and Pt/C were activated and cleaned in Ar-saturated 1 M KOH until a stable cyclic voltammetry (CV) curve was obtained. Figure 3a shows the representative hydrogen adsorption and desorption on Pt in Ptc/Ti₃C₂T_x and Pt/C. Obviously, the electrochemical surface area (ECSA) of Ptc/Ti₃C₂T_x is lower than that of Pt/C, which may be ascribed to the low loading of Pt clusters (4.1 wt % determined by inductively coupled plasma-optical emission spectroscopy, ICP-OES). Interestingly, Ptc/Ti₃C₂T_x shows lower hydrogen adsorption/desorption and oxygen adsorption/desorption potential than Pt/C. It means that the Pt species in Ptc/Ti₃C₂T_x prefer to bind OH⁻ rather than H⁺. Introducing 1 M methanol, Ptc/Ti₃C₂T_x and Pt/C each display one anodic peak, respectively, during the forward and reverse scanning (Figure 3b), corresponding to the respective oxidation process of methanol and its intermediates. Notably, Ptc/Ti₃C₂T_x

demonstrates a maximum current density of 38 mA cm⁻² lower than that of Pt/C (73 mA cm⁻²), and the current density of Pts/Ti₃C₂T_x and Ti₃C₂T_x is negligible (Figure S9). Compared by the mass activity, Ptc/Ti₃C₂T_x achieves a mass-specific activity of 7.32 A mg_{Pt}⁻¹ (Figure 3c), nearly three times more than that of Pt/C (2.86 A mg_{Pt}⁻¹), which is the highest value among the currently recorded Pt-based electrocatalysts (Figure 3d and Table S1). Besides, the onset potential of Ptc/Ti₃C₂T_x is significantly lower than Pt/C, indicating the higher adsorption and activation ability of Ptc/Ti₃C₂T_x to methanol molecules.

Durability performance is a key issue that limits the practical application of Pt-based electrocatalysts, and most of them reported are subject to rapid deactivation within thousands of seconds (Table S1). Through an accelerated durability test, the current density of Ptc/Ti₃C₂T_x is slowly decreasing while that of Pt/C decreases rapidly with the CV cycles increasing (Figure 3e). After 100 CV cycles, 69% of the initial maximum current density could be reserved for Ptc/Ti₃C₂T_x, much better than Pt/C (35%). Long-term operation stability was verified by chronoamperometric (*i*-*t*) at -0.1 V vs Hg/HgO.

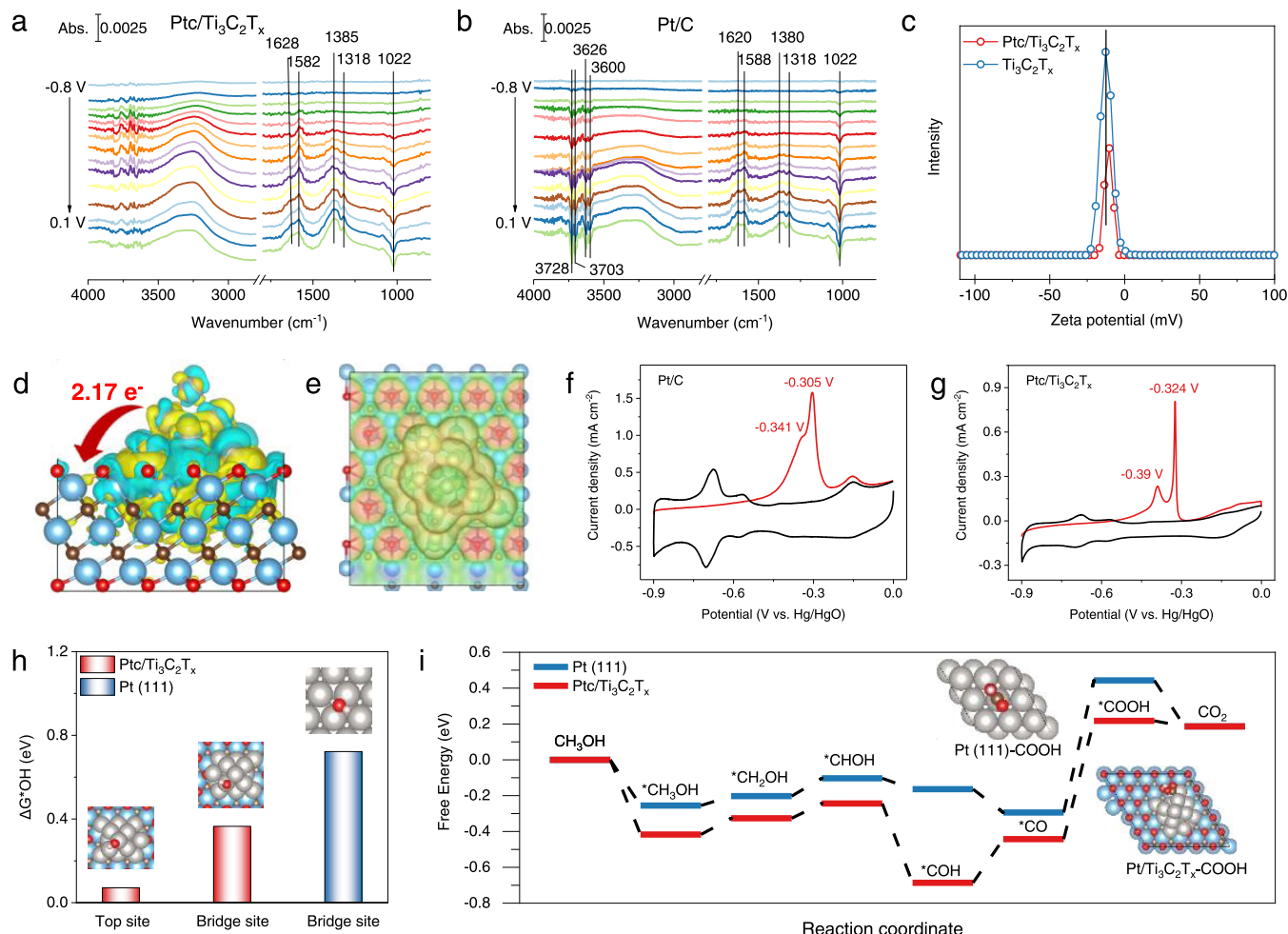


Figure 4. (a, b) In situ ATR-IR spectra under MOR operation for (a) Ptc/Ti₃C₂T_x and (b) Pt/C. (c) ζ potential tests of Ptc/Ti₃C₂T_x and Ti₃C₂T_x. (d) Charge density difference, where the yellow and blue areas denote the electron accumulation and depletion on Ptc/Ti₃C₂T_x. (e) Calculated electron density isosurfaces of Ptc/Ti₃C₂T_x, where the red and green areas denote the nucleophilic and electrostatic properties, respectively. The electron density isosurfaces are plotted at 0.002 e/Bohr³. (f, g) CO stripping experiments of (f) Pt/C and (g) Ptc/Ti₃C₂T_x. (h) Calculated *OH adsorption energy (ΔG^*_{OH}) on Ptc/Ti₃C₂T_x and Pt(111). (i) Free-energy profile of the methanol oxidation reaction on Ptc/Ti₃C₂T_x and Pt(111).

Within 100 min, the current density of Pt/C has lost over 80% (Figure 3f). However, Ptc/Ti₃C₂T_x retained a higher current density (95%) than Pt/C after the 100 min test, and 42% of the initial current density can be reserved even if the operative time is extended to 3000 min, indicating the high tolerance to CO poisoning. After the durability test, the Pt clusters on Ptc/Ti₃C₂T_x do not show obvious particle enlargement (Figure S10). These results indicate that benefitting from the structural stability and high CO oxidation rate, Ptc/Ti₃C₂T_x shows ultrahigh durability. The ECSA tests (Figures 3g and S11) show that Ptc/Ti₃C₂T_x possesses more ion adsorption sites. We believe that it is concerned with the interaction between Pt clusters and the Ti₃C₂T_x substrate.

Study on Reaction Mechanisms of Electrocatalysts. To further understand the origin of the high MOR performance of Ptc/Ti₃C₂T_x, we conducted in situ attenuated total reflection infrared (ATR-IR) spectroscopy and DFT calculations. Thin-film electrocatalyst electrodes were prepared and placed on the flat plane of a ZnSe hemicylindrical prism and pressed by a Ti rod (Figure S12). By collecting the evanescent wave signals, we successfully observed the variation of reaction intermediates. The ATR-IR proceeded in 1 M KOH aqueous solution with 1 M CH₃OH at the potential of

-0.8 to 0.1 V vs Ag/AgCl, and the acquired spectra are displayed in Figure 4a,b. A downward enhancement band at 1022 cm⁻¹ is detected in both Ptc/Ti₃C₂T_x and Pt/C, corresponding to the C-OH stretching vibration of methanol, and it can be attributed to the consumption of methanol. The C-OH and OCO symmetric stretching bands of *COOH (one of the reaction intermediates) between 1300 and 1400 cm⁻¹ are detected in Ptc/Ti₃C₂T_x at -0.3 V and enhance with increasing potential.^{50,51} Correspondingly, the correlation bands in Pt/C appear at -0.1 V, and the intensity at 0.1 V is lower than that of Ptc/Ti₃C₂T_x. The antisymmetric stretching vibration bands of OCO at 1580–1630 cm⁻¹ in Ptc/Ti₃C₂T_x are also higher and appear earlier than that of Pt/C. These results clearly confirm that Ptc/Ti₃C₂T_x possesses high absorption and activation capacity to methanol. It also noted that distinct negative-going bands at 3700–3730 cm⁻¹ are detected in Pt/C but not in Ptc/Ti₃C₂T_x. These bands can be assigned to the stretching mode of the O-H group (H₂O). Considering that the signal of the evanescent wave decreases with the increase of the penetration depth,⁵² the collected IR signal is mainly from the electrolyte rather than the electrode surface. Therefore, the appearance of O-H bands in Pt/C is attributed to the consumption of OH⁻ in electrolytes to

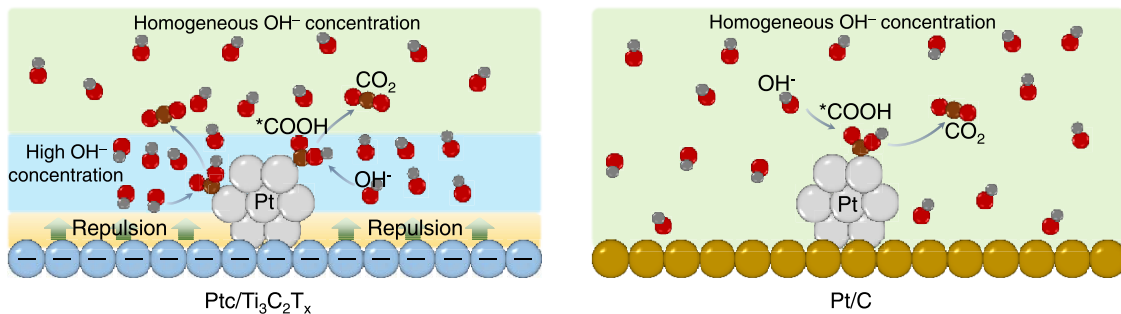


Figure 5. Schematic illustration of the proposed MOR mechanism on $\text{Ptc}/\text{Ti}_3\text{C}_2\text{T}_x$ and Pt/C .

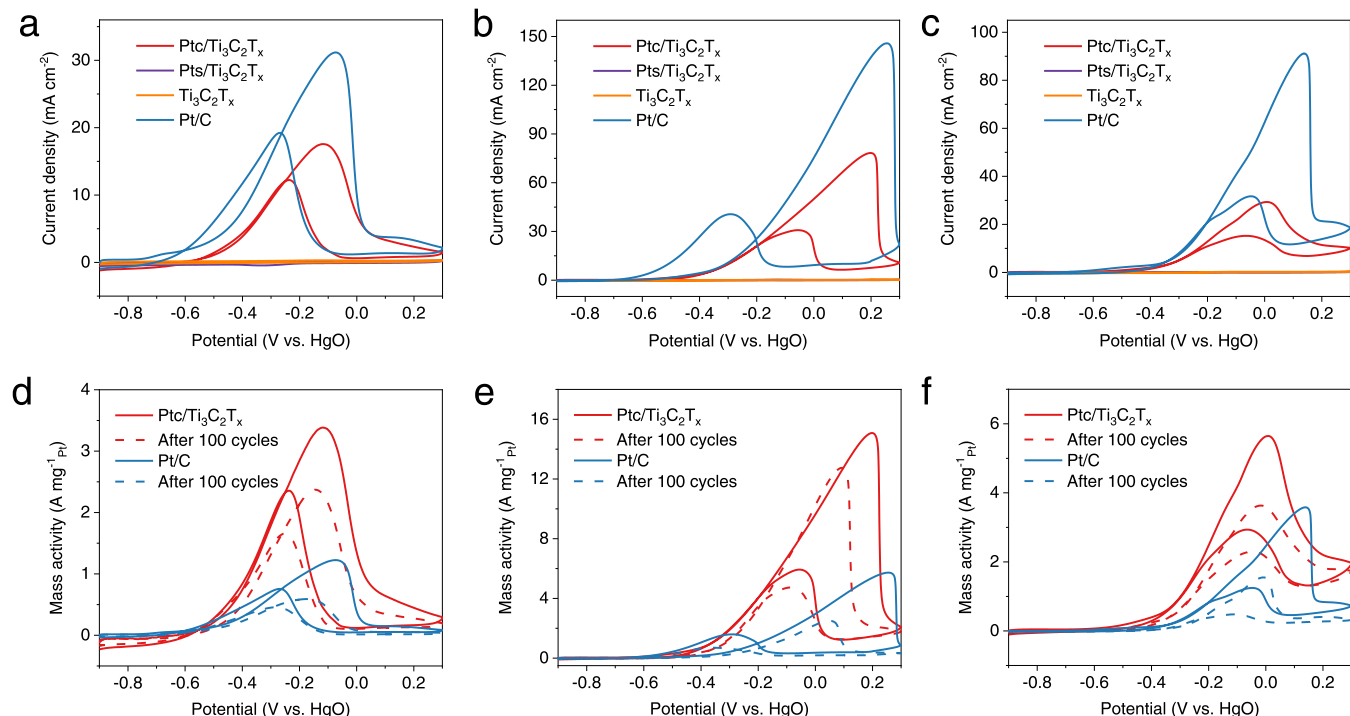


Figure 6. (a–c) CV curves of $\text{Ptc}/\text{Ti}_3\text{C}_2\text{T}_x$, $\text{Pts}/\text{Ti}_3\text{C}_2\text{T}_x$, $\text{Ti}_3\text{C}_2\text{T}_x$, and Pt/C in 1 M ethanol/1 M KOH (a), 1 M ethylene glycol/1 M KOH (b), and 1 M glycerol/1 M KOH (c). (d–f) Mass activity and durability test of $\text{Ptc}/\text{Ti}_3\text{C}_2\text{T}_x$, $\text{Pts}/\text{Ti}_3\text{C}_2\text{T}_x$, $\text{Ti}_3\text{C}_2\text{T}_x$, and Pt/C in 1 M ethanol/1 M KOH (d), 1 M ethylene glycol/1 M KOH (e), and 1 M glycerol/1 M KOH (f).

oxidize the CO_{ads} on the Pt/C surface. Conversely, CO_{ads} on $\text{Ptc}/\text{Ti}_3\text{C}_2\text{T}_x$ may be oxidized by OH^- near the surface of the electrode. Interestingly, ζ potential tests (Figure 4c) reveal the low OH^- concentration near the $\text{Ti}_3\text{C}_2\text{T}_x$ surface. Combining the results of in situ ATR-IR and ζ potential, it is speculated that a low OH^- concentration near the $\text{Ti}_3\text{C}_2\text{T}_x$ surface and a high OH^- concentration near the Pt cluster surface are formed.

DFT calculations were implemented to further comprehend the MOR reaction mechanism on $\text{Ptc}/\text{Ti}_3\text{C}_2\text{T}_x$ and Pt/C . First, we constructed the $\text{Ptc}/\text{Ti}_3\text{C}_2\text{T}_x$ and $\text{Pt}(111)$ models (Figures S13 and S14) to explore the activity of $\text{Ptc}/\text{Ti}_3\text{C}_2\text{T}_x$ and Pt/C catalysts. From the charge density difference displayed in Figure 4d, it can be seen that 2.17 electrons transfer from the Pt cluster to the $\text{Ti}_3\text{C}_2\text{T}_x$ substrate, indicating that the Pt cluster is positively charged, while the $\text{Ti}_3\text{C}_2\text{T}_x$ substrate is negatively charged. The electron-rich substrate may generate a strong surface electric field to repel the anions such as OH^- away from the $\text{Ti}_3\text{C}_2\text{T}_x$ surface, while the positively charged Pt clusters would attract OH^- to facilitate further oxidation of $^*\text{CO}$. It is further demonstrated in Figure 4e that OH^- can be easily adsorbed to the exposed Pt cluster

compared with the electron-rich $\text{Ti}_3\text{C}_2\text{T}_x$ surface, which facilitates the oxidation of $^*\text{CO}$ through binding OH^- from the aqueous medium. The CO resistance can be clearly explored by CO stripping voltammetry.⁵³ Figure 4f displays two typical oxidation peaks at -0.341 and -0.305 V in the first anodic scan for Pt/C , which can be attributed to the CO oxidation at different sites. Like Pt/C , $\text{Ptc}/\text{Ti}_3\text{C}_2\text{T}_x$ also bears two distinct CO oxidation peaks (Figure 4g), whereas the oxidation peaks are located at a lower potential (-0.39 and -0.324 V) with a smaller peak area. The lower CO adsorption capacity and onset potential suggest that CO is more weakly adsorbed on the surface of $\text{Ptc}/\text{Ti}_3\text{C}_2\text{T}_x$ and is more easy to be oxidized. These results reveal that $\text{Ptc}/\text{Ti}_3\text{C}_2\text{T}_x$ is capable of high tolerance to CO poisoning and thus exhibits ultrahigh MOR activity and durability.

To further verify the conjecture, we put a hydroxyl on the surface of $\text{Ptc}/\text{Ti}_3\text{C}_2\text{T}_x$ and $\text{Pt}(111)$ without applied potential. As shown in Figure 4h, the adsorption energy of OH^- on the Pt cluster of $\text{Ptc}/\text{Ti}_3\text{C}_2\text{T}_x$ is lower than that on $\text{Pt}(111)$. The hydroxyls consumed in the early stage of the reaction mainly come from the surface of the electrode, which is in great

agreement with the results of in situ ATR-IR. This certifies a strong attractive effect of Ptc/Ti₃C₂T_x for OH⁻ and thus accelerates the kinetics of OH⁻ transfer for further oxidizing CO_{ads} on Pt clusters. The MOR process, including *CH₃OH, *CH₂OH, *CHOH, *COH, *CO, and *COOH intermediates, is investigated on Ptc/Ti₃C₂T_x and Pt(111) displayed in Figures S13 and S14. The corresponding Gibbs free-energy profile is present in Figure 4i. We found that the addition of OH⁻ on *CO to form the *COOH intermediate is the rate-determining step (RDS) in the MOR.⁵⁴ Furthermore, the free-energy change of *COOH formation (0.66 eV) on Ptc/Ti₃C₂T_x is lower than 0.77 eV of Pt(111). Then, *COOH intermediates can be more easily oxidized to CO₂ on the Pt cluster of Ptc/Ti₃C₂T_x, which is consistent with CO stripping experiments. Therefore, with these theoretical calculations, it can be proved that Ptc/Ti₃C₂T_x has excellent catalytic performance for the MOR through kinetic and thermodynamic acceleration.

Based on the results of electrochemical tests, in situ characterizations, and theoretical calculations, we propose the mechanism of MOR that the strong surface electric field generated by the electron-rich Ti₃C₂T_x substrates produces repulsion between Ti₃C₂T_x and hydroxyls (Figure 5). The introduced repulsion promotes the migration of hydroxyls away from the Ti₃C₂T_x surface and results in a high local hydroxyl concentration around the anchored Pt clusters, thus enhancing the activated ability of Pt clusters to CO_{ads}. On the contrary, for the MOR catalyzed by Pt/C, the evenly distributed hydroxyls in electrolytes are free to take part in the MOR via the conventional Eley–Rideal mechanism. Consequently, Ptc/Ti₃C₂T_x exhibits higher MOR activity and durability than Pt/C.

Apart from the MOR, the activity of other alcohol oxidation reactions on Pt catalysts also suffer from CO poisoning.^{55,56} We further examined ethanol, ethylene glycol, and glycerol oxidation reaction (EOR, EGOR, and GOR) on Ptc/Ti₃C₂T_x. Surprisingly, Ptc/Ti₃C₂T_x also exhibits ultrahigh activity in these reactions. Although the area current densities of Ptc/Ti₃C₂T_x are lower than those of Pt/C (Figure 6a–c), the ultrahigh mass activity of 3.4, 15.1, and 5.6 A mg_{Pt}⁻¹ was recorded for EOR, EGOR, and GOR, respectively (Figure 6d–f). Moreover, Ptc/Ti₃C₂T_x maintains 71, 84, and 64% of the initial mass activity after 100 cycles of CV test for EOR, EGOR, and GOR, respectively. By contrast, Pt/C only retains 49, 43, and 42% of initial mass activity, further verifying the high activated capacity to CO_{ads} in Ptc/Ti₃C₂T_x.

CONCLUSIONS

In summary, combining theoretical and experimental results, we have successfully introduced a surface electric field to improve the resistance to CO poisoning of Pt clusters of Ptc/Ti₃C₂T_x catalysts and ultrahigh activity and durability for the MOR have been achieved. Due to the charge transfer from Pt clusters to Ti₃C₂T_x substrates, a strong electric field is generated on the surface of electron-rich Ti₃C₂T_x and then produces an interface repulsion. The field-induced repulsion leads to a high local hydroxyl concentration around the Pt clusters and promotes the CO_{ads} activation. In addition, the 3D crumpled ball structure suppresses the stacking of Ti₃C₂T_x and enlarges the contact area between catalysts and electrolytes, ensuring the effect of the electric field. The high activity and durability of Ptc/Ti₃C₂T_x to other alcohol oxidation reactions also confirm the enhancement effect of field-induced repulsion

to the CO tolerance. Constructing high local hydroxyl concentration on the electrocatalyst surface is a promising strategy for a small molecule oxidation reaction involving CO poisoning, and the effectiveness under industrial conditions needs to be further explored.

ASSOCIATED CONTENT

Supporting Information

The Supporting Information is available free of charge at <https://pubs.acs.org/doi/10.1021/jacs.2c03982>.

Experimental section; computational methods; SEM images; TEM images; HAADF-STEM image; XPS spectra; peak fitting analyses of Pt L₃-edge XANES spectra; CV curves; schematic and optical photographs of in situ ATR-IR; structural models; comparison of MOR performance of Ptc/Ti₃C₂T_x with Pt-based electrocatalysts recently reported ([PDF](#))

AUTHOR INFORMATION

Corresponding Authors

Liqiang Mai – State Key Laboratory of Advanced Technology for Materials Synthesis and Processing, Wuhan University of Technology, Wuhan 430070 Hubei, P. R. China; Foshan Xianhu Laboratory of the Advanced Energy Science and Technology Guangdong Laboratory, Foshan 528200, P. R. China;  orcid.org/0000-0003-4259-7725; Email: mlq518@whut.edu.cn

Ziyun Wang – School of Chemical Sciences, The University of Auckland, Auckland 1010, New Zealand;  orcid.org/0000-0002-2817-8367; Email: ziyun.wang@auckland.ac.nz

Authors

Jixin Zhu – State Key Laboratory of Advanced Technology for Materials Synthesis and Processing, Wuhan University of Technology, Wuhan 430070 Hubei, P. R. China;  orcid.org/0000-0003-1629-240X

Lixue Xia – International School of Materials Science and Engineering, Wuhan University of Technology, Wuhan 430070 Hubei, P. R. China;  orcid.org/0000-0001-6006-4055

Ruohan Yu – State Key Laboratory of Advanced Technology for Materials Synthesis and Processing, Wuhan University of Technology, Wuhan 430070 Hubei, P. R. China

Ruihu Lu – School of Chemical Sciences, The University of Auckland, Auckland 1010, New Zealand; International School of Materials Science and Engineering, Wuhan University of Technology, Wuhan 430070 Hubei, P. R. China;  orcid.org/0000-0001-8405-5962

Jiantao Li – State Key Laboratory of Advanced Technology for Materials Synthesis and Processing, Wuhan University of Technology, Wuhan 430070 Hubei, P. R. China

Ruhan He – State Key Laboratory of Advanced Technology for Materials Synthesis and Processing, Wuhan University of Technology, Wuhan 430070 Hubei, P. R. China

Yucai Wu – State Key Laboratory of Advanced Technology for Materials Synthesis and Processing, Wuhan University of Technology, Wuhan 430070 Hubei, P. R. China

Wei Zhang – State Key Laboratory of Advanced Technology for Materials Synthesis and Processing, Wuhan University of Technology, Wuhan 430070 Hubei, P. R. China

Xufeng Hong – State Key Laboratory of Advanced Technology for Materials Synthesis and Processing, Wuhan University of Technology, Wuhan 430070 Hubei, P. R. China
Wei Chen – State Key Laboratory of Advanced Technology for Materials Synthesis and Processing, Wuhan University of Technology, Wuhan 430070 Hubei, P. R. China; Hubei Key Laboratory of Ferro & Piezoelectric Materials and Devices, Hubei University, Wuhan 430062 Hubei, P. R. China
Yan Zhao – International School of Materials Science and Engineering, Wuhan University of Technology, Wuhan 430070 Hubei, P. R. China; orcid.org/0000-0002-1234-4455
Liang Zhou – State Key Laboratory of Advanced Technology for Materials Synthesis and Processing, Wuhan University of Technology, Wuhan 430070 Hubei, P. R. China; Foshan Xianhu Laboratory of the Advanced Energy Science and Technology Guangdong Laboratory, Foshan 528200, P. R. China; orcid.org/0000-0001-6756-3578

Complete contact information is available at:
<https://pubs.acs.org/10.1021/jacs.2c03982>

Author Contributions

#J.Z., L.X., and R.Y. contributed equally to this work.

Notes

The authors declare no competing financial interest.

ACKNOWLEDGMENTS

This work was supported by the National Key Research and Development Program of China (2020YFA0715000), National Natural Science Foundation of China (51832004, 51521001, 52127816), Foshan Xianhu Laboratory of the Advanced Energy Science and Technology Guangdong Laboratory (XHT2020-003), Open Project Fund of Hubei Provincial Key Laboratory of Ferroelectric Materials and Devices (K202003), and Fundamental Research Funds for the Central Universities (195101005, 2020III004GX). The authors thank the Beamline 12-BM-B at the Advanced Photon Source for XAFS measurement. This S/TEM work was performed at the Nanostructure Research Center (NRC), which is supported by the State Key Laboratory of Advanced Technology for Materials Synthesis and Processing and the State Key Laboratory of Silicate Materials for Architectures. The computational study was supported by the Marsden Fund Council from Government funding, managed by Royal Society Te Apārangi. Z.W. and R.L. wish to acknowledge the use of New Zealand eScience Infrastructure (NeSI) high-performance computing facilities, consulting support, and/or training services as part of this research. New Zealand's national facilities are provided by NeSI and funded jointly by NeSI's collaborator institutions and through the Ministry of Business, Innovation & Employment's Research Infrastructure programme. URL <https://www.nesi.org.nz>.

REFERENCES

- (1) Seh, Z. W.; Kibsgaard, J.; Dickens, C. F.; Chorkendorff, I. B.; Nørskov, J. K.; Jaramillo, T. F. Combining theory and experiment in electrocatalysis: Insights into materials design. *Science* **2017**, *355*, No. eaad4998.
- (2) Anson, C. W.; Stahl, S. S. Mediated fuel cells: soluble redox mediators and their applications to electrochemical reduction of O₂ and oxidation of H₂, alcohols, biomass, and complex fuels. *Chem. Rev.* **2020**, *120*, 3749–3786.
- (3) Luo, M.; Zhao, Z.; Zhang, Y.; Sun, Y.; Xing, Y.; Lv, F.; Yang, Y.; Zhang, X.; Hwang, S.; Qin, Y.; Ma, J.; Lin, F.; Su, D.; Lu, G.; Guo, S. PdMo bimetallic for oxygen reduction catalysis. *Nature* **2019**, *574*, 81–85.
- (4) Wan, X.; Liu, X.; Li, Y.; Yu, R.; Zheng, L.; Yan, W.; Wang, H.; Xu, M.; Shui, J. Fe–N–C electrocatalyst with dense active sites and efficient mass transport for high-performance proton exchange membrane fuel cells. *Nat. Catal.* **2019**, *2*, 259–268.
- (5) Zhou, Y.; Xie, Z.; Jiang, J.; Wang, J.; Song, X.; He, Q.; Ding, W.; Wei, Z. Lattice-confined Ru clusters with high CO tolerance and activity for the hydrogen oxidation reaction. *Nat. Catal.* **2020**, *3*, 454–462.
- (6) Zhuang, Z.; Li, Y.; Li, Y.; Huang, J.; Wei, B.; Sun, R.; Ren, Y.; Ding, J.; Zhu, J.; Lang, Z.; Moskaleva, L.; He, C.; Wang, Y.; Wang, Z.; Wang, D.; Li, Y. Atomically dispersed nonmagnetic electron traps improve oxygen reduction activity of perovskite oxides. *Energy Environ. Sci.* **2021**, *14*, 1016–1028.
- (7) Feng, Y.; Liu, H.; Yang, J. A selective electrocatalyst-based direct methanol fuel cell operated at high concentrations of methanol. *Sci. Adv.* **2017**, *3*, No. e1700580.
- (8) Wang, Y.-C.; Huang, L.; Zhang, P.; Qiu, Y.-T.; Sheng, T.; Zhou, Z.-Y.; Wang, G.; Liu, J.-G.; Rauf, M.; Gu, Z.-Q.; Wu, W.; Sun, S. Constructing a triple-phase interface in micropores to boost performance of Fe/N/C catalysts for direct methanol fuel cells. *ACS Energy Lett.* **2017**, *2*, 645–650.
- (9) Sharma, S.; Pollet, B. G. Support materials for PEMFC and DMFC electrocatalysts—a review. *J. Power Sources* **2012**, *208*, 96–119.
- (10) Hunt, S. T.; Milina, M.; Alba-Rubio, A. C.; Hendon, C. H.; Dumesic, J. A.; Román-Leshkov, Y. Self-assembly of noble metal monolayers on transition metal carbide nanoparticle catalysts. *Science* **2016**, *352*, 974–978.
- (11) Liu, L.; Corma, A. Metal catalysts for heterogeneous catalysis: from single atoms to nanoclusters and nanoparticles. *Chem. Rev.* **2018**, *118*, 4981–5079.
- (12) Jiang, J.; Ding, W.; Li, W.; Wei, Z. Freestanding single-atom-layer Pd-based catalysts: oriented splitting of energy bands for unique stability and activity. *Chem* **2020**, *6*, 431–447.
- (13) Liu, D.; Li, X.; Chen, S.; Yan, H.; Wang, C.; Wu, C.; Haleem, Y. A.; Duan, S.; Lu, J.; Ge, B.; Ajayan, P.; Luo, Y.; Jiang, J.; Song, L. Atomically dispersed platinum supported on curved carbon supports for efficient electrocatalytic hydrogen evolution. *Nat. Energy* **2019**, *4*, S12–S18.
- (14) Zhuang, Z.; Li, Y.; Yu, R.; Xia, L.; Yang, J.; Lang, Z.; Zhu, J.; Huang, J.; Wang, J.; Wang, Y.; Fan, L.; Wu, J.; Zhao, Y.; Wang, D.; Li, Y. Reversely trapping atoms from a perovskite surface for high-performance and durable fuel cell cathodes. *Nat. Catal.* **2022**, *5*, 300–310.
- (15) Bu, L.; Zhang, N.; Guo, S.; Zhang, X.; Li, J.; Yao, J.; Wu, T.; Lu, G.; Ma, J.-Y.; Su, D.; Huang, X. Biaxially strained PtPb/Pt core/shell nanoplate boosts oxygen reduction catalysis. *Science* **2016**, *354*, 1410–1414.
- (16) Greeley, J.; Stephens, I. E. L.; Bondarenko, A. S.; Johansson, T. P.; Hansen, H. A.; Jaramillo, T. F.; Rossmeisl, J.; Chorkendorff, I.; Nørskov, J. K. Alloys of platinum and early transition metals as oxygen reduction electrocatalysts. *Nat. Chem.* **2009**, *1*, 552–556.
- (17) Huang, L.; Zhang, X.; Wang, Q.; Han, Y.; Fang, Y.; Dong, S. Shape-control of Pt–Ru nanocrystals: tuning surface structure for enhanced electrocatalytic methanol oxidation. *J. Am. Chem. Soc.* **2018**, *140*, 1142–1147.
- (18) Gao, D.; Yang, S.; Xi, L.; Risch, M.; Song, L.; Lv, Y.; Li, C.; Li, C.; Chen, G. External and Internal Interface-Controlled Trimetallic PtCuNi Nanoframes with High Defect Density for Enhanced Electrooxidation of Liquid Fuels. *Chem. Mater.* **2020**, *32*, 1581–1594.
- (19) Li, M.; Duanmu, K.; Wan, C.; Cheng, T.; Zhang, L.; Dai, S.; Chen, W.; Zhao, Z.; Li, P.; Fei, H.; Zhu, Y.; Yu, R.; Luo, J.; Zang, K.; Lin, Z.; Ding, M.; Huang, J.; Sun, H.; Guo, J.; Pan, X.; Goddard, W., III; Sautet, P.; Huang, Y.; Duan, X. Single-atom tailoring of platinum

- nanocatalysts for high-performance multifunctional electrocatalysis. *Nat. Catal.* **2019**, *2*, 495–503.
- (20) Xiao, Y.-X.; Ying, J.; Tian, G.; Zhang, X.-Q.; Janiak, C.; Ozoemena, K. I.; Yang, X.-Y. PtPd hollow nanocubes with enhanced alloy effect and active facets for efficient methanol oxidation reaction. *Chem. Commun.* **2021**, *57*, 986–989.
- (21) Li, H.-H.; Fu, Q.-Q.; Xu, L.; Ma, S.-Y.; Zheng, Y.-R.; Liu, X.-J.; Yu, S.-H. Highly crystalline PtCu nanotubes with three dimensional molecular accessible and restructured surface for efficient catalysis. *Energy Environ. Sci.* **2017**, *10*, 1751–1756.
- (22) Wang, L.; Tian, X. L.; Xu, Y.; Zaman, S.; Qi, K.; Liu, H.; Xia, B. Y. Engineering one-dimensional and hierarchical PtFe alloy assemblies towards durable methanol electrooxidation. *J. Mater. Chem. A* **2019**, *7*, 13090–13095.
- (23) Zhang, W.; Yang, Y.; Huang, B.; Lv, F.; Wang, K.; Li, N.; Luo, M.; Chao, Y.; Li, Y.; Sun, Y.; Xu, Z.; Qin, Y.; Yang, W.; Zhou, J.; Du, Y.; Su, D.; Guo, S. Ultrathin PtNiM (M = Rh, Os, and Ir) nanowires as efficient fuel oxidation electrocatalytic materials. *Adv. Mater.* **2019**, *31*, No. 1805833.
- (24) Pan, Y.; Li, H.; Wang, Z.; Han, Y.; Wu, Z.; Zhang, X.; Lai, J.; Wang, L.; Feng, S. High-efficiency methanol oxidation electrocatalysts realized by ultrathin PtRuM–O (M = Ni, Fe, Co) nanosheets. *Chem. Commun.* **2020**, *56*, 9028–9031.
- (25) Xu, Y.; Cui, X.; Wei, S.; Zhang, Q.; Gu, L.; Meng, F.; Fan, J.; Zheng, W. Highly active zigzag-like Pt-Zn alloy nanowires with high-index facets for alcohol electrooxidation. *Nano Res.* **2019**, *12*, 1173–1179.
- (26) Tao, L.; Xia, Z.; Zhang, Q.; Sun, Y.; Li, M.; Yin, K.; Gu, L.; Guo, S. Spiny Pd/PtFe core/shell nanotubes with rich high-index facets for efficient electrocatalysis. *Sci. Bull.* **2021**, *66*, 44–51.
- (27) Li, C.; Chen, X.; Zhang, L.; Yan, S.; Sharma, A.; Zhao, B.; Kumbhar, A.; Zhou, G.; Fang, J. Synthesis of Core@Shell Cu-Ni@Pt-Cu Nano-Octahedra and Their Improved MOR Activity. *Angew. Chem.* **2021**, *133*, 7753–7758.
- (28) Huang, W.; Wang, H.; Zhou, J.; Wang, J.; Duchesne, P. N.; Muir, D.; Zhang, P.; Han, N.; Zhao, F.; Zeng, M.; Zhong, J.; Jin, C.; Li, Y.; Lee, S.-T.; Dai, H. Highly active and durable methanol oxidation electrocatalyst based on the synergy of platinum–nickel hydroxide–graphene. *Nat. Commun.* **2015**, *6*, No. 10035.
- (29) Zhao, X.; Yin, M.; Ma, L.; Liang, L.; Liu, C.; Liao, J.; Lu, T.; Xing, W. Recent advances in catalysts for direct methanol fuel cells. *Energy Environ. Sci.* **2011**, *4*, 2736–2753.
- (30) Yang, C.; Jiang, Q.; Li, W.; He, H.; Yang, L.; Lu, Z.; Huang, H. Ultrafine Pt nanoparticle-decorated 3D hybrid architectures built from reduced graphene oxide and MXene nanosheets for methanol oxidation. *Chem. Mater.* **2019**, *31*, 9277–9287.
- (31) Wang, X.; Xi, S.; Lee, W. S. V.; Huang, P.; Cui, P.; Zhao, L.; Hao, W.; Zhao, X.; Wang, Z.; Wu, H.; Wang, H.; Diao, C.; Borgna, A.; Du, Y.; Yu, Z.; Pennycook, S.; Xue, J. Materializing efficient methanol oxidation via electron delocalization in nickel hydroxide nanoribbon. *Nat. Commun.* **2020**, *11*, No. 4647.
- (32) Anasori, B.; Lukatskaya, M. R.; Gogotsi, Y. 2D metal carbides and nitrides (MXenes) for energy storage. *Nat. Rev. Mater.* **2017**, *2*, No. 16098.
- (33) Zhang, J.; Zhao, Y.; Guo, X.; Chen, C.; Dong, C.-L.; Liu, R.-S.; Han, C.-P.; Li, Y.; Gogotsi, Y.; Wang, G. Single platinum atoms immobilized on an MXene as an efficient catalyst for the hydrogen evolution reaction. *Nat. Catal.* **2018**, *1*, 985–992.
- (34) Li, Z.; Zhuang, Z.; Lv, F.; Zhu, H.; Zhou, L.; Luo, M.; Zhu, J.; Lang, Z.; Feng, S.; Chen, W.; Mai, L.; Guo, S. The marriage of the FeN₄ moiety and MXene boosts oxygen reduction catalysis: Fe 3d electron delocalization matters. *Adv. Mater.* **2018**, *30*, No. 1803220.
- (35) Zhao, D.; Chen, Z.; Yang, W.; Liu, S.; Zhang, X.; Yu, Y.; Cheong, W.-C.; Zheng, L.; Ren, F.; Ying, G.; Cao, X.; Wang, D.; Peng, Q.; Wang, G.; Chen, C. MXene (Ti₃C₂) vacancy-confined single-atom catalyst for efficient functionalization of CO₂. *J. Am. Chem. Soc.* **2019**, *141*, 4086–4093.
- (36) Wang, X.; Mathis, T. S.; Li, K.; Lin, Z.; Vlcek, L.; Torita, T.; Osti, N. C.; Hatter, C.; Urbankowski, P.; Sarycheva, A.; et al. Influences from solvents on charge storage in titanium carbide MXenes. *Nat. Energy* **2019**, *4*, 241–248.
- (37) Li, Y.; Shao, H.; Lin, Z.; Lu, J.; Liu, L.; Dupoyer, B.; Persson, P. O.; Eklund, P.; Hultman, L.; Li, M.; Chen, K.; Zha, X.; Du, S.; Rozier, P.; Chai, Z.; Raymundo-Piñero, E.; Taberna, P.-L.; Simon, P.; Huang, Q. A general Lewis acidic etching route for preparing MXenes with enhanced electrochemical performance in non-aqueous electrolyte. *Nat. Mater.* **2020**, *19*, 894–899.
- (38) Lukatskaya, M. R.; Kota, S.; Lin, Z.; Zhao, M.-Q.; Shpigel, N.; Levi, M. D.; Halim, J.; Taberna, P.-L.; Barsoum, M. W.; Simon, P.; Gogotsi, Y. Ultra-high-rate pseudocapacitive energy storage in two-dimensional transition metal carbides. *Nat. Energy* **2017**, *2*, No. 17105.
- (39) Wu, Y.; Wei, W.; Yu, R.; Xia, L.; Hong, X.; Zhu, J.; Li, J.; Lv, L.; Chen, W.; Zhao, Y.; Zhou, L.; Mai, L. Anchoring Sub-Nanometer Pt Clusters on Crumpled Paper-Like MXene Enables High Hydrogen Evolution Mass Activity. *Adv. Funct. Mater.* **2022**, *32*, No. 2110910.
- (40) Sang, X.; Xie, Y.; Lin, M.-W.; Alhabeb, M.; Van Aken, K. L.; Gogotsi, Y.; Kent, P. R. C.; Xiao, K.; Unocic, R. R. Atomic defects in monolayer titanium carbide (Ti₃C₂T_x) MXene. *ACS Nano* **2016**, *10*, 9193–9200.
- (41) Alhabeb, M.; Maleski, K.; Mathis, T. S.; Sarycheva, A.; Hatter, C. B.; Uzun, S.; Levitt, A.; Gogotsi, Y. Selective etching of silicon from Ti₃SiC₂ (MAX) to obtain 2D titanium carbide (MXene). *Angew. Chem.* **2018**, *130*, 5542–5546.
- (42) Xia, Y.; Mathis, T. S.; Zhao, M.-Q.; Anasori, B.; Dang, A.; Zhou, Z.; Cho, H.; Gogotsi, Y.; Yang, S. Thickness-independent capacitance of vertically aligned liquid-crystalline MXenes. *Nature* **2018**, *557*, 409–412.
- (43) Troyano, J.; Çamur, C.; Garzón-Tovar, L.; Carné-Sánchez, A.; Imaz, I.; Maspoch, D. Spray-drying synthesis of MOFs, COFs, and related composites. *Acc. Chem. Res.* **2020**, *53*, 1206–1217.
- (44) Dai, Y.; Gorey, T. J.; Anderson, S. L.; Lee, S.; Lee, S.; Seifert, S.; Winans, R. E. Inherent size effects on XANES of nanometer metal clusters: size-selected platinum clusters on silica. *J. Phys. Chem. C* **2017**, *121*, 361–374.
- (45) Natu, V.; Benchakar, M.; Canaff, C.; Habrioux, A.; Celerier, S.; Barsoum, M. W. A critical analysis of the X-ray photoelectron spectra of Ti₃C₂T_x MXenes. *Matter* **2021**, *4*, 1224–1251.
- (46) Li, Z.; Chen, Y.; Ji, S.; Tang, Y.; Chen, W.; Li, A.; Zhao, J.; Xiong, Y.; Wu, Y.; Gong, Y.; Yao, T.; Liu, W.; Zheng, L.; Dong, J.; Wang, Y.; Zhuang, Z.; Xing, W.; He, C.-T.; Peng, C.; Cheong, W.-C.; Li, Q.; Zhang, M.; Chen, Z.; Fu, N.; Gao, X.; Zhu, W.; Wan, J.; Zhang, J.; Gu, L.; Wei, S.; Hu, P.; Luo, J.; Li, J.; Chen, C.; Peng, Q.; Duan, X.; Huang, Y.; Chen, X.-M.; Wang, D.; Li, Y. Iridium single-atom catalyst on nitrogen-doped carbon for formic acid oxidation synthesized using a general host–guest strategy. *Nat. Chem.* **2020**, *12*, 764–772.
- (47) Han, A.; Zhang, J.; Sun, W.; Chen, W.; Zhang, S.; Han, Y.; Feng, Q.; Zheng, L.; Gu, L.; Chen, C.; Peng, Q.; Wang, D.; Li, Y. Isolating contiguous Pt atoms and forming Pt-Zn intermetallic nanoparticles to regulate selectivity in 4-nitrophenylacetylene hydrogenation. *Nat. Commun.* **2019**, *10*, No. 3787.
- (48) Lin, L.; Zhou, W.; Gao, R.; Yao, S.; Zhang, X.; Xu, W.; Zheng, S.; Jiang, Z.; Yu, Q.; Li, Y.-W.; Shi, C.; Wen, X.-D.; Ma, D. Low-temperature hydrogen production from water and methanol using Pt/α-MoC catalysts. *Nature* **2017**, *544*, 80–83.
- (49) Li, H.; Han, Y.; Zhao, H.; Qi, W.; Zhang, D.; Yu, Y.; Cai, W.; Li, S.; Lai, J.; Huang, B.; Wang, L. Fast site-to-site electron transfer of high-entropy alloy nanocatalyst driving redox electrocatalysis. *Nat. Commun.* **2020**, *11*, No. 5437.
- (50) Yajima, T.; Uchida, H.; Watanabe, M. In situ ATR-FTIR spectroscopic study of electro-oxidation of methanol and adsorbed CO at Pt–Ru alloy. *J. Phys. Chem. B* **2004**, *108*, 2654–2659.
- (51) Zhou, Y.-W.; Chen, Y.-F.; Jiang, K.; Liu, Z.; Mao, Z.-J.; Zhang, W.-Y.; Lin, W.-F.; Cai, W.-B. Probing the enhanced methanol electrooxidation mechanism on platinum-metal oxide catalyst. *Appl. Catal., B* **2021**, *280*, No. 119393.

- (52) Zhu, S.; Li, T.; Cai, W.-B.; Shao, M. CO₂ electrochemical reduction as probed through infrared spectroscopy. *ACS Energy Lett.* **2019**, *4*, 682–689.
- (53) Xiong, Y.; Dong, J.; Huang, Z.-Q.; Xin, P.; Chen, W.; Wang, Y.; Li, Z.; Jin, Z.; Xing, W.; Zhuang, Z.; Ye, J.; Wei, X.; Cao, R.; Gu, L.; Sun, S.; Zhuang, L.; Chen, X.; Yang, H.; Chen, C.; Peng, Q.; Chang, C.-R.; Wang, D.; Li, Y. Single-atom Rh/N-doped carbon electrocatalyst for formic acid oxidation. *Nat. Nanotechnol.* **2020**, *15*, 390–397.
- (54) Xiong, L.; Sun, Z.; Zhang, X.; Zhao, L.; Huang, P.; Chen, X.; Jin, H.; Sun, H.; Lian, Y.; Deng, Z.; Rümmeli, M. H.; Yin, W.; Zhang, D.; Wang, S.; Peng, Y. Octahedral gold-silver nanoframes with rich crystalline defects for efficient methanol oxidation manifesting a CO-promoting effect. *Nat. Commun.* **2019**, *10*, No. 3782.
- (55) Wu, D.; Kusada, K.; Yamamoto, T.; Toriyama, T.; Matsumura, S.; Kawaguchi, S.; Kubota, Y.; Kitagawa, H. Platinum-Group-Metal High-Entropy-Alloy Nanoparticles. *J. Am. Chem. Soc.* **2020**, *142*, 13833–13838.
- (56) Matsuoka, K.; Iriyama, Y.; Abe, T.; Matsuoka, M.; Ogumi, Z. Electro-oxidation of methanol and ethylene glycol on platinum in alkaline solution: Poisoning effects and product analysis. *Electrochim. Acta* **2005**, *51*, 1085–1090.

□ Recommended by ACS

Moving beyond Ti₂C₃T_x MXene to Pt-Decorated TiO₂@TiC Core–Shell via Pulsed Laser in Reshaping Modification for Accelerating Hydrogen Evolution Kinetics

Chae Eun Park, Myong Yong Choi, et al.

MARCH 06, 2023

ACS NANO

READ ▶

Ultrathin Nanotube Structure for Mass-Efficient and Durable Oxygen Reduction Reaction Catalysts in PEM Fuel Cells

Jieyuan Liu, Jianglan Shui, et al.

OCTOBER 05, 2022

JOURNAL OF THE AMERICAN CHEMICAL SOCIETY

READ ▶

Pt@Metal–Organic Framework (ZIF-8) Thin Films Obtained at a Liquid/Liquid Interface as Anode Electrocatalysts for Methanol Fuel Cells: Different Appro...

Golandam Askarisarvestani, Wei Chen, et al.

JULY 26, 2022

INORGANIC CHEMISTRY

READ ▶

Facile Solid-State Synthesis of Supported PtNi and PtCo Bimetallic Nanoparticles for the Oxygen Reduction Reaction

Alexander Gunnarson, Ferdi Schüth, et al.

FEBRUARY 28, 2023

CHEMISTRY OF MATERIALS

READ ▶

Get More Suggestions >